3D Reconstruction of Dinoflagellate Chromosomes from Hi-C Data Refutes the Cholesteric Liquid Crystal Hypothesis

Lucas Philipp[1], **Georgi K. Marinov**[2], **Stephen Todd**[3,4], **and Stephanie C. Weber**[1,5,*]

This manuscript was compiled on January 24, 2025

Dinoflagellates contain permanently condensed chromosomes that are often described as liquid crystalline. Specifically, a Cholesteric Liquid Crystal (CLC) model was proposed in which DNA is organized into parallel fibers within stacked discs, such that the fiber orientation rotates by a constant angle between adjacent discs. Extrachromosomal loops extending from the discs were hypothesized to be more accessible and thus to contain transcriptionally active genes. Although the CLC model captures some features of dinoflagellate chromosome structure, its validity has not been rigorously tested against modern genomic data. Here, we use chromatin conformation capture (Hi-C) data to simulate 3D conformations of chromosome scaffolds for two dinoflagellate species, *Symbiodinium kawagutii* and *Symbiodinium microadriaticum*. These polymer conformations are compact helices with significant orientational and nematic order. However, we find no evidence of cholesteric discs. Moreover, simulated Hi-C contact maps of CLC structures lack topologically associating domains (TADs), which are observed in experimental Hi-C contact maps for these species. Finally, by mapping RNA-seq data onto our simulated conformations, we show that actively transcribed genes are present throughout the entire chromosome, and not exclusively on extrachromosomal loops or at the surface. Our results refute the long-standing CLC model and suggest that dinoflagellate chromosomes are organized into condensed but non-crystalline structures that do not impede transcription.

dinoflagellate | chromosome conformation capture | transcription | topologically associating domain | liquid crystal

Significance Statement

Dinoflagellates have permanently condensed chromosomes that are structurally unique among eukaryotes. These chromosomes are often described as cholesteric liquid crystals (CLCs). In this article, we generate three-dimensional polymer conformations from chromatin conformation capture (Hi-C) data. Our results indicate that, while dinoflagellate chromosomes are organized into compact helical structures, they do not contain parallel stacks of flat discs and are therefore not CLCs. Mapping RNA-seq data onto our simulated conformations reveals actively transcribed genes throughout the entire chromosome, contradicting CLC model predictions and raising questions as to the role of condensation and extrachromosomal loops in regulating gene expression.

Dinoflagellates are a diverse group of unicellular algae whose chromosomes remain highly condensed throughout the cell cycle (1). How this unusual chromosome structure impacts gene expression is a longstanding question, since compact chromatin domains typically exclude RNA polymerase (2, 3) and suppress transcription (4) in other eukaryotes. The leading hypothesis to explain both the unique structure of dinoflagellate chromosomes and its consequences for transcription is the cholesteric liquid crystal (CLC) model. Originally proposed over fifty years ago, the CLC model posits that DNA is packaged into a series of flat discs that stack to form the long axis of the chromosome (5). Within each disc, chromatin fibers are arranged parallel to a director that rotates a constant angle between discs (6–9) (Fig. 1 A). The CLC geometry is consistent with banding patterns observed in 2D transmission electron micrographs (5, 6). In addition, extrachromosomal loops were hypothesized to connect adjacent and non-adjacent discs (SI Appendix, Fig. S1 A) and to contain transcriptionally-active genes, due to their presumed greater accessibility compared to the condensed chromosome core (5–8, 10–15). Though often assumed to be true, the validity of the CLC model and its predictions for the spatial organization of transcription have not been rigorously tested against modern genomic data.

Chromosome conformation capture (Hi-C) is an experimental sequencing technique that measures which regions of primary DNA sequence contact each other in three-dimensional space. Hi-C analysis of several dinoflagellate species (16–18) revealed topologically associating domains (TADs), regions of primary sequence that interact with each other at much higher probabilities than with other chromosomal regions. These "dinoTADs" correlate with another common feature of dinoflagellate genomes, tandem arrays of co-oriented genes (19–22). Indeed, the insulation boundaries that separate dinoTADs occur at locations where two oppositely-oriented gene arrays converge (16, 17). Moreover, these boundaries are disrupted by transcription inhibitors, suggesting that active transcription may contribute to dinoTAD formation. Nevertheless, it remains unclear whether

Author affiliations: [1]Quantitative Life Sciences Program, McGill University, Montreal, Canada; [2]Department of Genetics, Stanford University, Palo Alto, USA; [3]Department of Computing, Goldsmiths, University of London, London, United Kingdom; [4]London Geometry Ltd., London, United Kingdom; [5]Departments of Biology and Physics, McGill University, Montreal, Canada

L.P. and S.C.W. designed the research, wrote the paper, and obtained funding; G.K.M. improved the *S. kawagutii* genome assembly using raw Hi-C reads, assembled *S. kawagutii* contact maps, and aligned RNA-seq reads to the genome; S.T. added data visualization and manual TAD annotation functionalities to CSynth; L.P. performed all other research aspects.

The authors declare no conflict of interest.

*To whom correspondence should be addressed. E-mail: steph.weber@mcgill.ca

DRAFT

dinoTADs correspond to cholesteric discs and whether the CLC model is consistent with Hi-C data more generally.

In this article, we use previously published Hi-C data (16, 18) to simulate 3D conformations of chromosome scaffolds from two dinoflagellate species: *Symbiodinium kawagutii* (recently re-named *Fugacium kawagutii* (23)), and *Symbiodinium microadriaticum*. Surprisingly, our results indicate that dinoflagellate chromosomes are not organized into a stack of cholesteric discs as predicted by the CLC model. Rather, they are helical, with orientational and nematic order that is greater than equilibrium globules (a confined 3D random walk), but less than CLCs. By mapping RNA-seq reads (24–26) onto our simulated polymer conformations, we find that active genes are located throughout the chromosome and not solely on the surface. This distribution suggests that although dinoflagellate chromosomes are highly condensed, they remain accessible to RNA polymerase. Our findings clarify important aspects of dinoflagellate chromosome structure and resolve a long-standing question as to how this structure relates to transcriptional activity.

Results

Dinoflagellate chromosomes lack cholesteric discs. We used CSynth (27) to compute the 3D conformation of DNA within dinoflagellate chromosomes that best reproduces empirical Hi-C contact probabilities. We validated this approach in two different ways. First, we generated a set of CLC structures with known monomer positions to serve as a positive control (Fig. 1 A, SI Appendix, Fig. S1). We calculated Hi-C contact maps from these CLC structures and fed them into CSynth. The CSynth-generated output conformations consist of a rotating stack of ordered discs and have a 7% relative error in monomer pairwise separation compared to the known input CLCs (SI Appendix, Fig. S2). Second, we used empirical Hi-C (28) and fluorescence in situ hybridization (FISH) (29) datasets for chromosome 21 in human IMR90 cells to determine the optimal parameter set that minimizes the relative error between the pairwise separation predicted by CSynth and real distances measured by light microscopy (652 FISH probes spaced 50 kb apart) (SI Appendix, Fig. S3). The optimized parameter set was used to simulate conformations for all *S. kawagutii* (SI Appendix, Fig. S4) and *S. microadriaticum* (SI Appendix, Fig. S5) chromosome scaffolds at 5 kb per monomer resolution.

In contrast to the CLC model, 3D conformations of dinoflagellate chromosomes lack cholesteric discs (Fig. 1 A). Instead, they are organized into helices, which is especially apparent at a coarser resolution of 100 kb per monomer (Fig. 1 B). We observed few extrachromosomal loops in *S. kawagutii* (0.63 per chromosome, $N = 75$) (SI Appendix, Fig. S4) and *S. microadriaticum* (1.78 per chromosome, $N = 75$) (SI Appendix, Fig. S5). Extrachromosomal loops were previously reported to be between 30-60 kb in length (30), corresponding to 6-12 monomers per loop in our simulations. Therefore, the apparent sparseness of extrachromosomal loops is not due to limited resolution. *S. microadriaticum* chromosomes are on average more elongated than *S. kawagutii* chromosomes (1.4 times longer than wide, versus 1.2) (SI Appendix, Fig. S4 & S5). Neither species exhibited conformations resembling cholesteric discs in which the polymer is oriented approximately parallel.

In addition to the observed conformational differences between dinoflagellate chromosomes and the CLC model, simulated Hi-C contact maps of CLCs with variable extrachromosomal loops are qualitatively different from empirical dinoflagellate Hi-C contact maps (SI Appendix, S1 B). The most striking difference is the lack of TADs in simulated Hi-C contact maps of CLC structures (Fig. 1 C). Previous research has shown that, in some living systems, TADs can arise from chromosome conformational heterogeneity across individual cells (32). To rule out this possibility, we explicitly modeled conformational heterogeneity by generating an ensemble of 10^6 CLC structures, approximating the number of cells sequenced in a typical bulk Hi-C experiment, with random extrachromosomal loop lengths and positions. However, even with this structural heterogeneity, the simulated contact map for the CLC model does not reproduce TADs (Fig. 1 C).

Instead, the simulated Hi-C contact map for CLCs contains stripes of high-contact probability that are ∼parallel and perpendicular to the central diagonal, creating a grid-like pattern. The number of stripes is determined by the number of cholesteric discs in the input structures (SI Appendix, Fig. S6). Therefore, the absence of these stripes in empirical Hi-C contact maps indicates a lack of cholesteric discs in dinoflagellate chromosomes. Moreover, the presence of TADs in empirical Hi-C data is not consistent with the CLC model and cannot be explained by random extrachromosomal loops. This conclusion is robust to changing CLC model parameters, such as the percentage of total sequence in extrachromosomal loops, the number of cholesteric discs, and the cholesteric pitch (SI Appendix, Fig. S6). Furthermore, TADs are not reproduced in simulated Hi-C contact maps when the number of cholesteric discs per chromosome is randomized across individual CLC structures (SI Appendix, Fig. S6).

Dinoflagellate contact probability curves are inconsistent with CLC model predictions. Contact probability curves are often used to describe chromosome organizational features (33). This metric quantifies how frequently any two DNA loci, separated by a fixed amount of primary sequence, make contact in 3D space. Mathematically, contact probability can be written as $P(s = |i-j| * 5 \text{ kb}) \propto \sum_{|i-j|*5 \text{ kb}=s} \frac{CP_{Hi-C,ij}}{L-s} \propto s^{\gamma}$ where $\sum_{|i-j|*5 \text{ kb}=s} CP_{Hi-C,ij}$ is the sum of Hi-C contact probabilities for all monomer pairs (i, j) separated by $s = |i-j|*5$ kb, L is the chromosome length, and γ is the contact probability decay exponent. The exact proportionality depends on the Hi-C normalization procedure. The decay exponent can be compared across species and to predictions from various models (33). For example, equilibrium globules have a decay exponent of $\gamma = -1.5$, while human interphase chromosomes have a decay exponent of $\gamma = -1$ (33).

To determine the decay exponent expected from the CLC model, we calculated the contact probability curve for an ensemble of CLC structures following the methods outlined in (34). For intermediate genomic separations, $s = 10^4 - 10^6$ bp, $P(s)$ is very shallow with a decay exponent of $\gamma \approx -0.2$, (Fig. 2 A). This exponent is robust across a range of CLC parameters (SI Appendix, Fig. S6), reflecting the high degree of compaction in this polymer model. At larger genomic separations, $s > 10^6$ bp, the curve decays more rapidly, consistent with the linear stacking of cholesteric discs. Furthermore, contact probability curves for CLCs

DRAFT

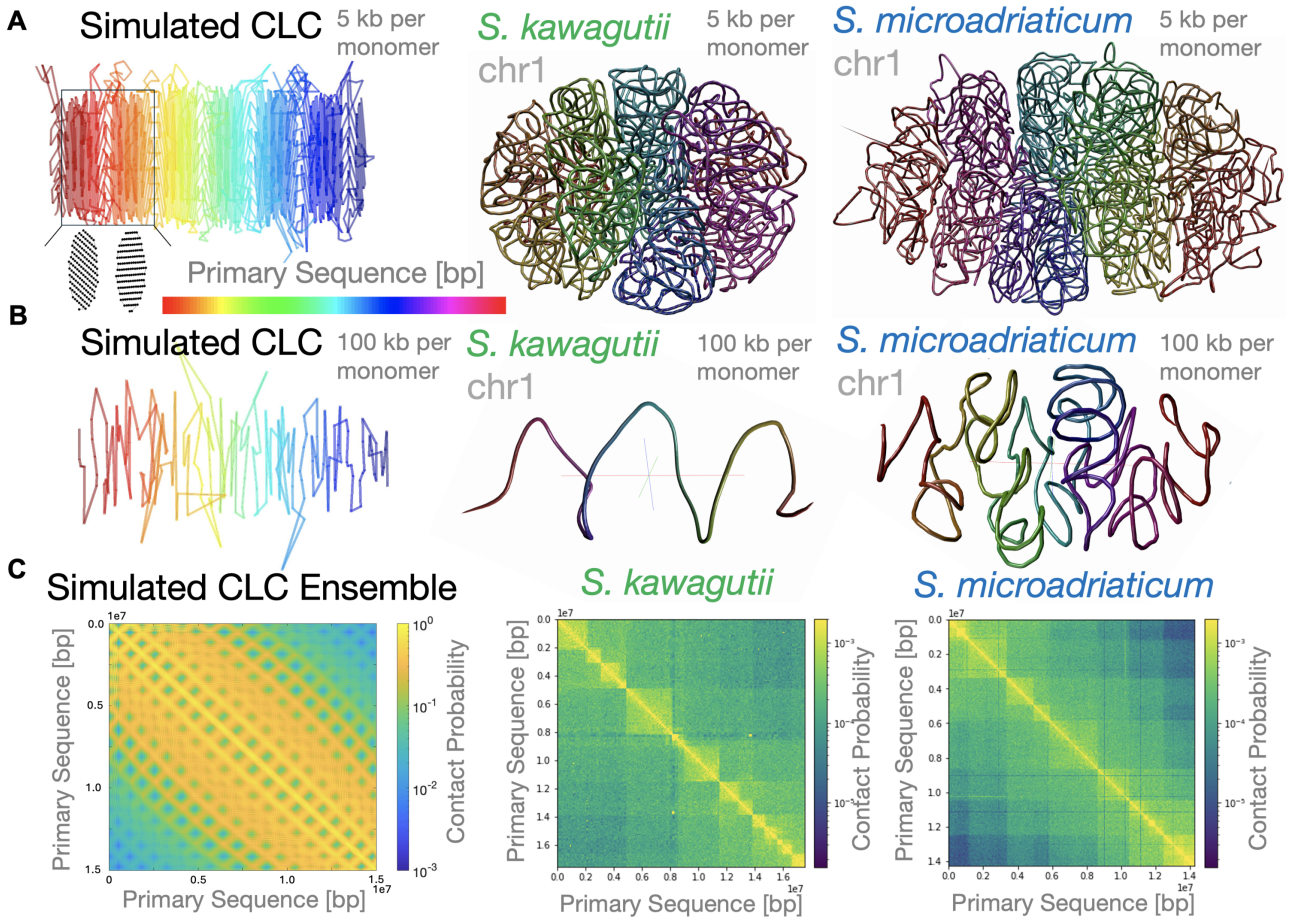

Fig. 1. Dinoflagellate chromosomes lack cholesteric discs. A) CSynth conformations at 5 kb per monomer resolution of a simulated CLC, a *Symbiodinium kawagutii* chromosome scaffold (Hi-C data: (18, 31)), and a *Symbiodinium microadriaticum* chromosome scaffold (Hi-C data: (16)). For complete set of dinoflagellate chromosome scaffolds, see SI Appendix, Figures S4 & S5. Color indicates primary sequence. Inset of CLC structure shows polymer orientation within two cholesteric discs. Local director rotates a constant angle between adjacent discs. B) CSynth conformations of the same chromosomes in A) at 100 kb per monomer resolution. C) Left: Simulated Hi-C contact map for an ensemble of 10^6 CLC structures, lacking topologically associating domains. Middle & Right: Empirical Hi-C contact maps of representative dinoflagellate chromosomes ((16, 18)) with clear topologically associating domains.

have two prominent local maxima at genomic separations corresponding to intra-disc ($\sim 10^5$ bp) and inter-disc ($\sim 10^6$ bp) contacts (vertical dashed lines: Fig. 2 A, SI Appendix, Fig. S6).

Next, we calculated contact probability curves for *S. kawagutii* and *S. minutum* (for which Hi-C scaffolds are not chromosome-length, SI Appendix, Table 1), as was done previously for *S. microadriaticum* (16), using the cooltools package (35). $P(s)$ curves for dinoflagellate chromosome scaffolds are smooth, with a decay exponent of $\gamma \approx -0.5$ (Fig. 2 B-D). This power-law scaling is steeper than what we observed for the CLC model (Fig. 2 A, SI Appendix, Fig. S6), suggesting that dinoflagellate chromosomes are less condensed than CLCs. Moreover, these contact probability curves have no peaks at intermediate genomic separations, as would be expected for cholesteric discs. Overall, we find no evidence of cholesteric organization in the contact probability curves of dinoflagellate chromosome scaffolds.

DinoTADs are structurally diverse, unlike cholesteric discs. Given the apparent absence of cholesteric discs, we next focused on dinoTADs, which are the most prominent feature in empirical Hi-C contact maps (Fig. 1 C) (16, 17). We developed a manual TAD annotation tool within the CSynth GUI which allows the user to select the apex of a TAD with a mouse click and then automatically writes the left and right TAD boundary base-pair coordinates to a text file (Fig. 3 A, Methods). As with the rest of CSynth, this tool runs in a web browser and does not require any software installation (27). Moreover, it can be used to annotate TADs in hundreds of chromosomes in less than an hour. These TAD annotations can be used to visualize multiple TADs in distinct colors on the same 3D chromosome (Fig. 3 B, Methods). Our manual TAD annotation tool has many advantages over existing automatic TAD annotators, which can be sensitive to parameter choice, involve lengthy computation times, require installation, or may not support integrated visualization of their output (36).

We used this new tool to annotate dinoTADs in Hi-C datasets (16, 18). A majority of the genome - 84% in *S. kawagutii* and 71% in *S. microadriaticum* - is organized into dinoTADs, which are located throughout our CSynth conformations but not in a regular arrangement or stack (Fig. 3 B). In a CLC, every cholesteric disc has the same

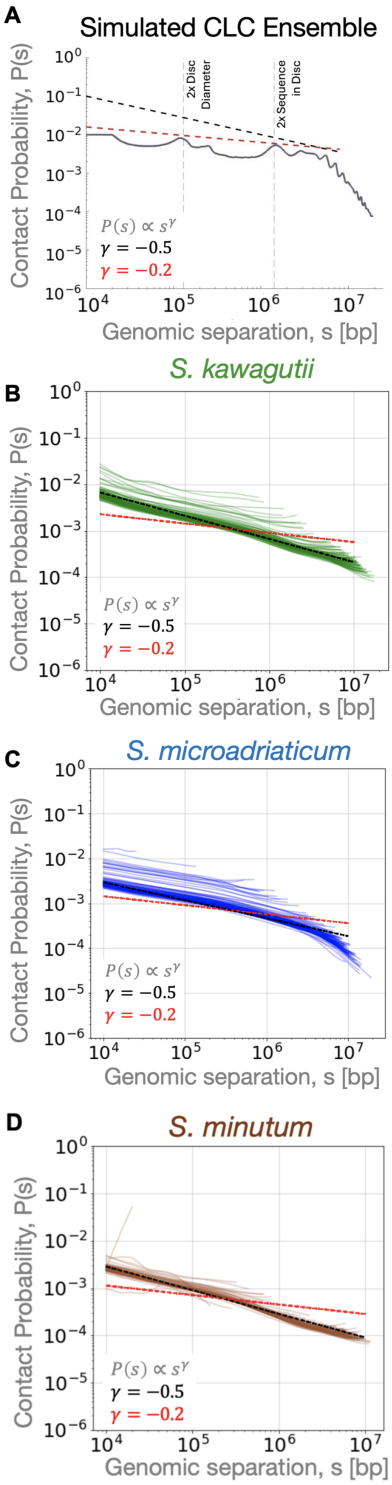

Fig. 2. Contact probability curves for dinoflagellate chromosomes are inconsistent with CLC model predictions. A) Contact probability curve for an ensemble of 10^6 CLC structures. The genomic separation corresponding to twice the cholesteric disc diameter and to two cholesteric discs are indicated by vertical dashed lines. Black dashed lines represent a power law relationship with an exponent $\gamma \approx -0.5$. Red dashed lines represent a power law with exponent $\gamma \approx -0.2$. Contact probability curves for the 75 largest B) *Symbiodinium kawagutii* chromosome scaffolds. C) *Symbiodinium microadriaticum* chromosome scaffolds (data: (16)). D) *Symbiodinium minutum* chromosome scaffolds (data: (17)). Each curve corresponds to an individual chromosome scaffjols.

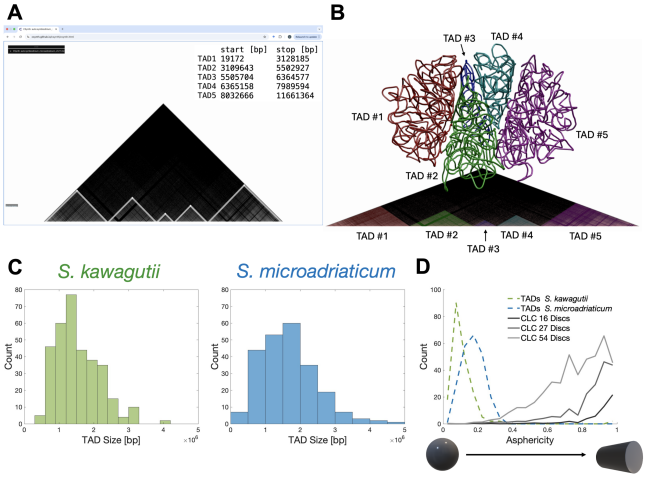

Fig. 3. DinoTADs are structurally diverse, unlike cholesteric discs. A) CSynth allows for rapid manual annotation of TADs and generates a text file of boundary coordinates (inset). B) TADs can be visualized as distinct colors on the Hi-C contact map (bottom triangle) and in the 3D polymer conformation. C) Distribution of dinoTAD sizes in *S. kawagutii* and *S. microadriaticum*. D) Asphericity of dinoTADs and cholesteric discs from CLCs with varying total number of discs.

size and shape (Fig. 1, SI Appendix, Fig. S1). However, dinoTADs are variable in size, ranging from 0.32 Mb to 4.8 Mb, with an average of $\sim$ 1.5 Mb (Fig. 3 C). To compare the shapes of cholesteric discs and dinoTADs, we calculated the asphericity of each domain in our CSynth conformations, where an asphericity of 0 corresponds to a perfect sphere and an asphericity of 1 to a perfect rod (37). Cholesteric discs have a high asphericity, consistent with their flat shape (Fig. 3 D). The random extrachromosomal loops in our CSynth conformations introduce skew in the asphericity distributions. For a fixed polymer length, the total number of discs in a CLC inversely correlates with disc diameter, such that CLCs with fewer discs have wider and therefore more aspherical discs, which we see in our CSynth conformations. Compared to cholesteric discs, dinoTADs have very low asphericity (Fig. 3 D). Interestingly, dinoTADs in *S. kawagutii* have lower asphericity than dinoTADs in *S. microadriaticum* (Fig. 3 D), perhaps reflecting their smaller whole-chromosome aspect ratios (Fig. 1 A, SI Appendix, Fig. S4 & S5). The variable size and more rounded shape of dinoTADs may preclude crystalline ordering of DNA in dinoflagellate chromosomes.

Dinoflagellate chromosomes exhibit orientational and nematic order. To investigate how the structural heterogeneity of dinoTADs affects orientational order within dinoflagellate chromosomes, we calculated the orientation order parameter (OOP) (38) and its Fourier transform. The OOP can be defined as $OOP(|i-j| * 5 \text{ kb}) =< \vec{r}_i \cdot \vec{r}_j >$, where $\vec{r}_i$ is the unit tangent vector to the ith monomer, and the brackets $< \cdot >$ denote the average dot product over all possible pairs of monomers (i, j) separated by $|i-j| * 5$ kb base pairs. For helical organization, the OOP is a sinusoid as a function of primary sequence separation and its Fourier transform is a narrow peak corresponding to the period of the helix (Fig. 3 A).

We compared the OOPs of CLCs as a positive control; equilibrium globules as a negative control; and fine-grained (5 kb per monomer resolution) CSynth conformations of *S.*

kawagutii and *S. microadriaticum* chromosome scaffolds (Fig. 4 B). The OOP of CLC conformations exhibits a damped oscillation (Fig. 4 B, Row 1). Two sets of peaks are detected in its Fourier transform: one peak corresponds to orientational ordering between adjacent cholesteric discs ($\sim 10^{-6}$ 1/bp), and the other corresponds to orientational ordering within a cholesteric disc ($\sim 10^{-5}$ 1/bp). The location of these peaks depends on the average number of monomers in a cholesteric disc, and not on the percentage of sequence in extrachromosomal loops, as expected (SI Appendix, Fig. S7 A). Equilibrium globules are confined 3D random walks with no orientational order. We calculated the OOP of equilibrium globules using data from (33). As expected, the OOP monotonically decays at short genomic separations and plateaus to zero. There are no peaks in its Fourier transform, consistent with the lack of periodic structure (Fig. 4 B, Row 2).

In contrast, the OOPs for both *S. kawagutii* and *S. microadriaticum* lack both the oscillatory signature of the CLC model and the monotonic decay of the equilibrium globule. Instead, they exhibit a negative peak at $\sim 5 * 10^4$ bp (Fig. 4 B, Rows 3 & 4). This genomic separation corresponds to the average length of gene arrays in each species, suggesting that gene arrays may fold in an anti-parallel orientation.

Interestingly, we detect no orientational order on the scale of dinoTADs at this resolution, likely due to their structural heterogeneity. However, the OOP of coarse-grained (100 kb per monomer resolution) conformations of *S. kawagutii* and *S. microadriaticum* chromosome scaffolds show an undamped oscillation and its Fourier transform contains a prominent peak (SI Appendix, Fig. S7 B) near the size of dinoTADs. These results are consistent with the helical appearance of these coarse-grained conformations (Fig. 1 B) and indicate that dinoflagellate chromosomes are organized in a global helix.

Ordering of the chromatin fiber could also occur independently of primary sequence separation and instead depend on the 3D spatial proximity of DNA loci. To measure this, we calculated the local nematic order parameter (NOP) at two different scales following the methods outlined in (39) for the same set of conformations as above. For CLC conformations, the degree of nematic ordering is sensitive to voxel size and number of cholesteric discs (Fig. 4 C). For equilibrium globules, we found a negligible degree of nematic ordering, as expected. Finally, we observe a moderate degree of nematic ordering in dinoflagellate chromosome scaffolds, intermediate between that of CLCs and equilibrium globules. Altogether, both OOP and NOP metrics indicate that dinoflagellate chromosomes are more ordered than equilibrium globules, but not as ordered as expected for CLCs.

Active genes occur throughout dinoflagellate chromosomes. Finally, we visualized the 3D spatial distribution of active genes in dinoflagellate chromosomes by mapping RNA-seq reads (24–26) to the genome assembly, and in turn, onto their corresponding 3D locations as predicted by CSynth. Fig. 5 A shows the divergent color-map used to visualize strand-specific gene expression, with red/blue indicating the strand, darker shades of red/blue indicating higher transcription levels, and grey indicating regions where no transcripts were detected. The scale of our color-map is calibrated to capture the entire dynamic range of expression levels observed (SI Appendix, Fig. S8). If active transcription occurs primarily on extrachromosomal loops, as hypothesized by the CLC model (5–8, 10–15, 40–43), then we would expect a colorful chromosome surface and a grey chromosome core (Fig. 5 B). Instead, we observe that active genes are located throughout both *S. kawagutii* and *S. microadriaticum* chromosomes (Fig. 5 B), and not exclusively on the nucleoplasm-exposed surface. In fact, a majority ($> 50\%$) of the primary sequence of each chromosome is transcriptionally active, a fraction greater than what is accessible to RNA polymerase assuming up to 30% radial penetration from the surface (SI Appendix, Fig. S8). After hiding transcriptionally inactive regions of the chromosome, where no transcripts are detected, we observe that the remaining transcriptionally active regions are not enriched at the surface (Fig. 5 B), demonstrating that transcription is spatially ubiquitous.

Although active genes are present throughout dinoflagellate chromosomes, their relative expression levels may still depend on a gene's distance to the chromosome surface. We defined a cylindrical coordinate system where the cylindrical axis is the chromosome's long axis, and the radial axis is the perpendicular distance from the cylindrical axis to the chromosome's surface (Fig. 5 C). To determine whether transcription levels correlate with proximity to the surface, we used this coordinate system to calculate the average gene expression throughout *S. kawagutii* and *S. microadriaticum* chromosomes, controlling for variation in DNA density across voxels (Fig. 5 D, Methods).

The CLC model predicts that active transcription occurs on extrachromosomal loops, which are located at the chromosome surface, as opposed to the core, which is hypothesized to be inaccessible to RNA polymerases. Thus, we would expect to see the highest expression levels at the surface and low or no expression in the core (Fig. 5 D). In contrast to this expectation, we observe active genes throughout dinoflagellate chromosome scaffolds. Interestingly, we find somewhat increased transcription levels away from the center of the cylindrical axis (Fig. 5 D). Telomeres are also preferentially located away from the center of the cylindrical axis (SI Appendix, Fig. S9), which is consistent with the previous observation that *S. microadriaticum* chromosomes have higher gene density at their telomeres (16). Overall, we find no correlation between gene expression and radial position in dinoflagellate chromosomes, indicating that active transcription is not restricted to extrachromosomal loops.

Discussion

We determined the 3D conformations that best reproduce empirical Hi-C contact maps for chromosomes from two dinoflagellate species, *S. kawagutii* and *S. microadriaticum*. Our CSynth conformations have compact ellipsoidal shapes, in which the chromatin fiber winds helically from one end to the other (Fig. 1 A, SI Appendix, S4, S5). Along this helical path, the polymer "crumples" into a series of compact domains that correspond to dinoTADs (Fig. 1 C, 3 B). These features are in stark contrast to the CLC model, in which structures are cylindrical in shape and composed of a stack of flat discs, within which the chromatin fiber runs back and forth parallel to a director that rotates from one disc to the next (Fig. 1 A).

DRAFT

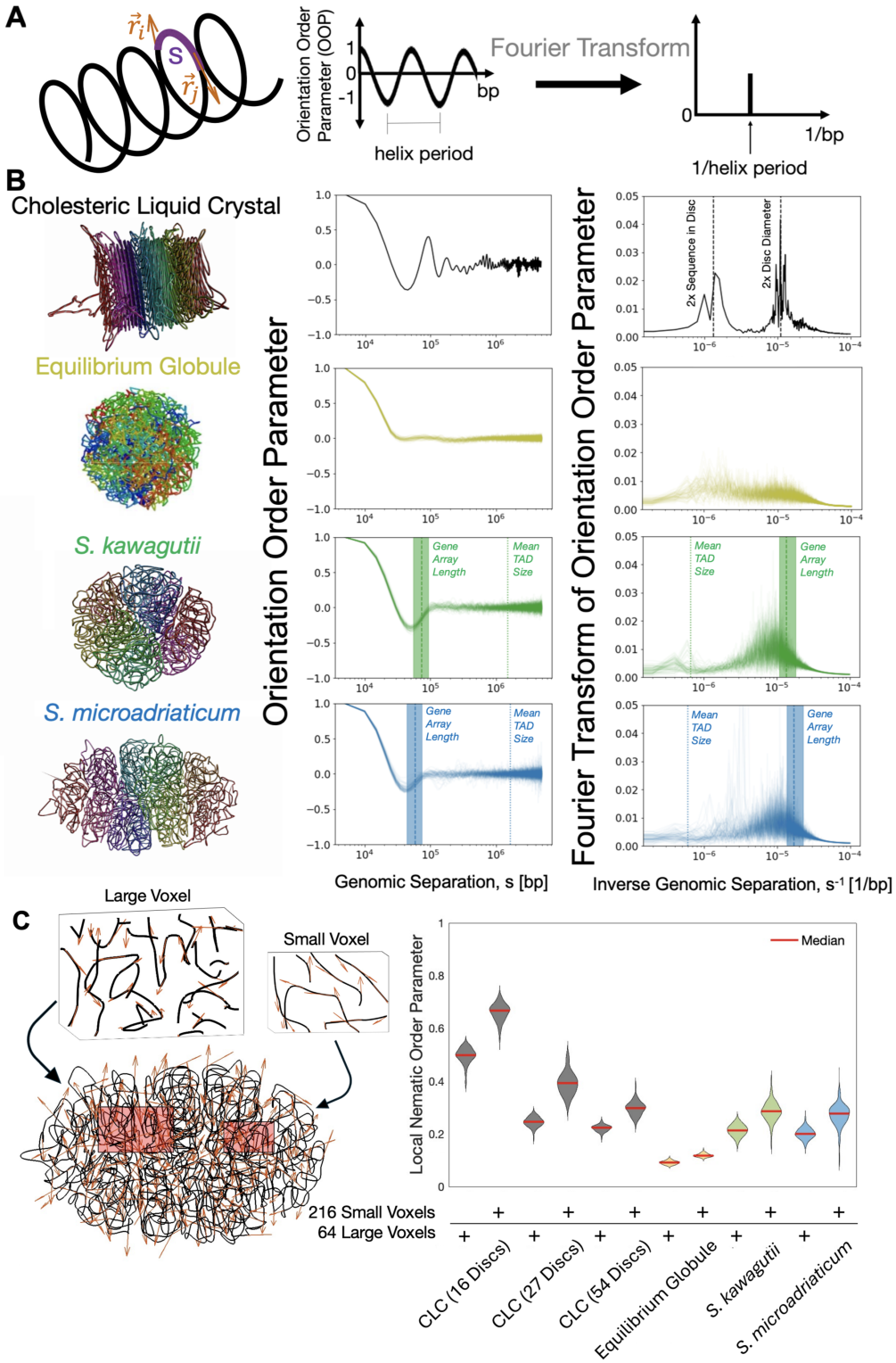

Fig. 4. Dinoflagellate chromosomes exhibit orientational and nematic order. A) Expected orientation order parameter (OOP), correlating tangent vectors (red arrows) as a function of primary sequence separation s (purple). OOP Fourier transform for a simple helix. B) Left: OOP. Right: Fourier transform of OOP. Row 1: CLC chromosome. Dashed lines: reciprocal of the average amount of sequence in two cholesteric discs, reciprocal of the amount of sequence in twice the average disc diameter. Row 2: Equilibrium globules (data: (33)). Each curve represents one of 75 conformations. Row 3: *S. kawagutii.* Each curve represents one of the 75 largest chromosomes. The mean gene array size (+/- 1 standard deviation), and the mean TAD size are indicated. Row 4: *S. microadriaticum.* Each curve represents one of the 75 largest chromosomes. The mean gene array size (+/- 1 standard deviation), and the mean TAD size are indicated. C) Left: Example dinoflagellate chromosome with DNA sequence (black) and tangent vectors (red arrows). Small and large voxels (red boxes) are blown-up in the insets. Right: The local nematic order parameter is calculated for all tangent vectors within each voxel. Different sized voxels are used representing short range and long range orientational order.

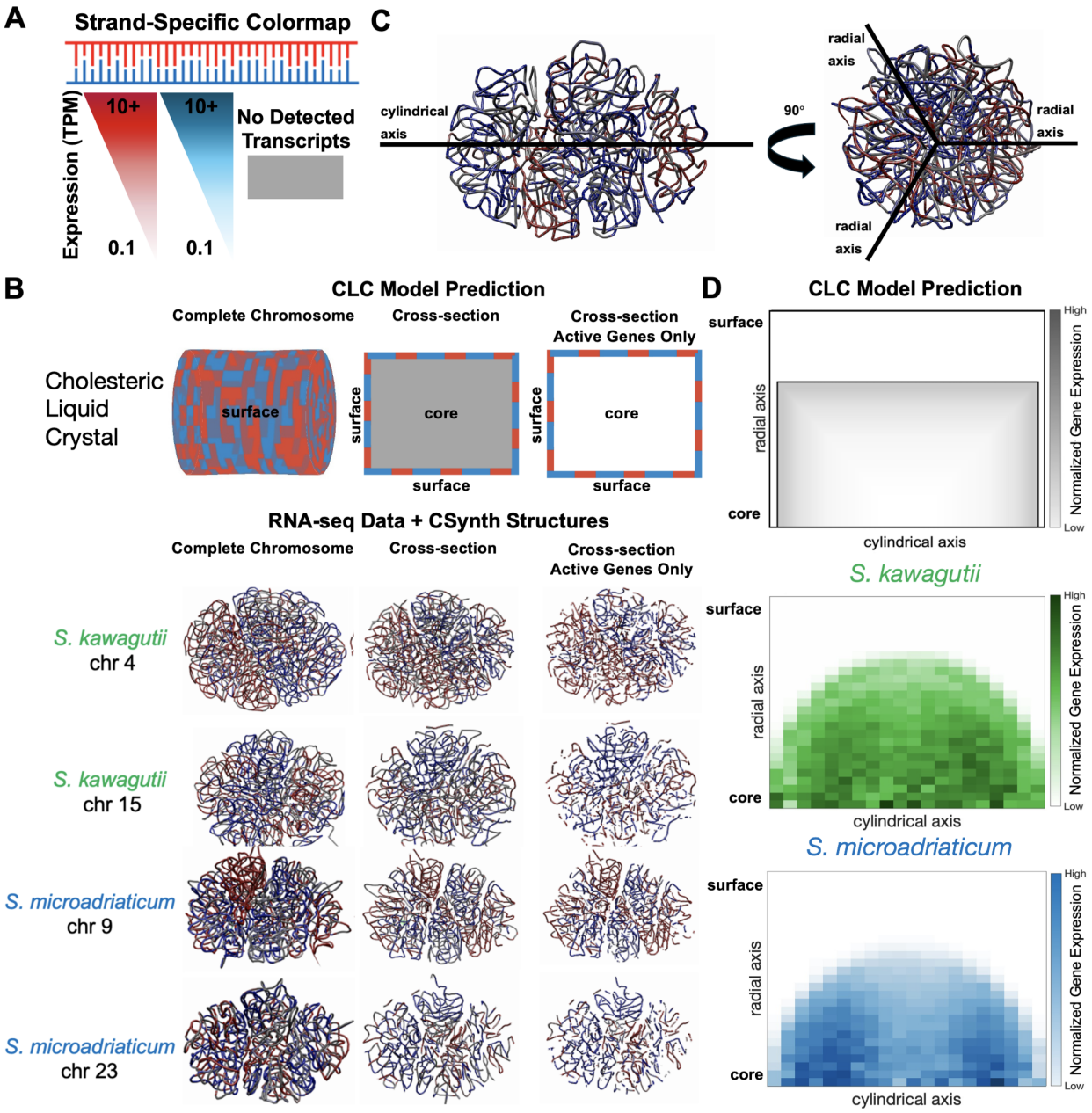

Fig. 5. Active genes occur throughout dinoflagellate chromosomes. A) Description of divergent color-map used to visualize strand-specific gene expression in 3D. In the CLC model, active genes are expected on the chromosome surface and not in the condensed core. B) Top: CLC model prediction of peripherally located active genes. Three views are shown: 1) the complete chromosome, 2) a cross-section exposing the chromosome core, 3) the same cross section hiding sequences containing no active genes. Bottom: RNA-seq reads (data: (24–26)) aligned to dinoflagellate genome assembly mapped onto CSynth 3D chromosome model. Randomly selected chromosomes are shown. C) Description of cylindrical coordinate system with cylindrical axis aligned with the chromosome long axis. The outward radial axis is perpendicular to the cylindrical axis. D) Azimuthally averaged active gene density as a function of distance to chromosome core (radial axis) and position along chromosome long axis (cylindrical axis). Top: In the CLC model active genes are hypothesized to be near the chromosome surface on extrachromosomal loops, and not in the condensed core. Middle/Bottom: The largest 75 chromosomes for each species (*S. kawagutii* = green, *S. microadriaticum* = blue) are scaled to the same size and superimposed.

These conformational differences lead to distinct patterns in Hi-C contact maps. Empirical Hi-C contact maps for *S. kawagutii* and *S. microadriaticum* are dominated by squares along the diagonal, which correspond to dinoTADs (Fig. 1 C, 3 B) (16, 17). However, the regular order of the polymer within and between discs in the CLC model results in stripes both parallel and perpendicular to the central diagonal in simulated Hi-C contact maps (Fig. 1 C).

The contact probability curves for reconstructed dinoflagellate chromosome conformations decay smoothly, with an exponent of $\gamma \approx -0.5$ (Fig. 2 B, C, D). In contrast, the contact probability curve for the CLC model has a much shallower decay, with an exponent of $\gamma \approx -0.2$, and is interrupted by peaks corresponding to intra-disc and inter-disc contacts (Fig. 2 A).

DinoTADs are variable in size and more spherical in shape than flat cholesteric discs (Fig. 3). Although these domains are not arranged into a regular stack, dinoflagellate chromosomes nevertheless have significant orientation and nematic order (Fig. 4).

The CLC model highlights the unique structure of dinoflagellate chromosomes relative to other eukaryotes. It successfully predicts a highly compact twisted chromosome, with significant orientational order. However, our systematic analysis of reconstructed conformations reveals several important disagreements between dinoflagellate chromosomes and the CLC model's predictions. Therefore, we conclude that dinoflagellate chromosomes (at least in these two species) are not cholesteric liquid crystals.

In addition to the CLC model, many other models for dinoflagellate chromosome organization have been proposed. One model consists of two independent helices coiled around each other (44). Another model consists of a toroidal chromosome twisted into a double helix, emphasizing rounded hairpin loops at the chromosome ends rather than exposed telomeres (45). A third model proposes that dinoflagellate chromosomes are polytene, i.e. they undergo many rounds of complete and/or partial replication without segregation, maintaining close alignment of sister chromatids (46). A fourth model consists of a hierarchical helix with six degrees of hierarchy (47, 48). A fifth model consists of a helical condensed core, with abundant extrachromosomal loops (49).

Our 3D conformations of dinoflagellate chromosomes are not consistent with any of these models. They do not consist of multiple interwoven helices, are not twisted toroids, are not helices of helices, and do not contain abundant extrachromosomal loops. Our 3D conformations have exposed telomere ends (SI Appendix, Fig. S9), rather than rounded hairpin loops. Furthermore, dinoflagellate Hi-C contact maps do not contain an X-shape pattern that is characteristic of circular chromosomes (50), do not have variable contact probability along the main diagonal as is the case for chromosomes with polytene bands (51), and lack significant trans-chromosomal contacts that would be expected from interwoven helices involving multiple chromosomes (16–18).

In addition to dinoflagellates, condensed, twisted, and ordered interphase chromosome structures have been observed in at least three other biological contexts: mosquito chromosomes (52), cricket sperm chromosomes (39), and bacterial nucleoids (53). The latter two examples are particularly interesting because they also lack nucleosomes, suggesting that these types of structures may be more common in the absence of histones. Histones are replaced by SNBPs (sperm-specific nuclear basic proteins) in sperm cells (39) and bacteria use a variety of nucleoid-associated proteins, including HU (heat unstable) proteins (54), to package their DNA. In dinoflagellates, dinoflagellate viral nuclear protein (DVNPs) and histone-like proteins (HLPs) replace histones (41, 42, 55).

Beyond DNA structure, the CLC model also makes functional predictions. Indeed, it predicts that active genes are located on the chromosome surface in extrachromosomal loops and not in the condensed chromosome core (5–8, 10–15, 40–43). These predictions are mainly based on radiolabeling studies, which show incorporation of ^{3}H-adenine or ^{3}H-uridine at the nucleolus (10, 11, 40), but not overlapping with chromosomes. Our results, which leverage modern genomic techniques, suggest that transcription is spatially ubiquitous. We find active genes throughout dinoflagellate chromosomes and not exclusively at the chromosome surface (Fig. 5 B & D). Our findings are consistent with other modern genomic assays such as ATAC-seq, which indicate that dinoflagellate genomes are uniformly accessible to transposases (56). Moreover, transcription still occurs in highly condensed human mitotic chromosomes (4). Thus, dinoflagellate chromosomes are likely accessible to RNA polymerase and condensation is not the primary mechanism for regulation of gene expression. Rather, dinoflagellate genes can be actively transcribed regardless of their chromosomal location.

Although our results indicate that chromosome conformation does not influence gene expression in dinoflagellates, transcription may contribute to chromosome organization. For example, we observe orientational order at length scales corresponding to gene arrays (Fig. 4 B). The negative peak in the OOP curve for dinoflagellate chromosomes is similar to that observed in model human chromosomes perturbed by extensible force dipoles that represent transcriptional activity (57). Thus, transcription of co-oriented genes in divergent gene arrays appears to result in an anti-parallel arrangement. Transcription has also been implicated in dinoTAD formation. Indeed, the boundaries of dinoTADs correspond to positions at which oppositely-oriented gene arrays converge in *S. microadriaticum* (16) and *S. minutum* (17) and are sensitive to transcriptional inhibitors. We mapped RNA-seq reads (24–26) onto the *S. kawagutii* genome assembly and also found that dinoTAD boundaries occur between convergent gene arrays (SI Appendix, Fig. S9 C), consistent with these previous studies (16, 17).

Many researchers have used transmission electron microscopy (TEM) to generate 2D cross-sectional images of dinoflagellate chromosomes (1, 5–8, 13, 58–62). To date, no study has imaged dinoflagellate chromatin fiber orientation in 3D. Instead, interpretation of the banding patterns observed in 2D cross-sectional images has relied on mathematically projecting 3D CLC models onto a 2D imaging plane (5). The limitation of 2D data makes it difficult to extrapolate ordering observed in a single plane to volumes within a whole chromosome, and to track the contours of individual chromatin fibers as a function of primary sequence. For example, dinoflagellate chromosomes that produced banding patterns in TEM cross-sections typically attributed to CLC organization, appear helical when viewed after a whole-

DRAFT

mounting procedure (63). In addition, a recent TEM study (61) found that while oblique and longitudinal sections of *Prorocentrum micans* chromosomes agree qualitatively with CLC model predictions, DNA fibers were not parallel within transverse sections - an observation that is inconsistent with cholesteric discs. The advantage of our Hi-C based polymer physics approach is that the entire dinoflagellate chromosome is modeled in 3D with the added context of primary sequence information.

Overall, this work advances our understanding of dinoflagellate chromosome organization in 3D, providing evidence that dinoflagellate chromosomes are not cholesteric liquid crystals. Further work should focus on 3D experimental imaging and chromatin fiber tracing within dinoflagellate chromosomes, as well as 3D imaging of nascent RNA and transcription (64).

Methods

Hi-C data pre-processing. Hi-C assisted genome assemblies and contact probabilities were accessed from the GEO with accession numbers: GSE152150 (16) and GSE153950 (17), or from the SRA with accession numbers: SRR25948349, SRR25948348 (31) and further processed following (18). All Hi-C data originated from asynchronous cell populations.

S. kawagutii Hi-C contact maps were converted from .hic format to .cool format using the hic2cool python package https://github.com/4dn-dcic/hic2cool.

When un-ligated and self-ligated Hi-C artifacts are abundant, Hi-C normalization can greatly reduce off-diagonal contact probabilities (65). This results in weak CSynth Hi-C-based attraction forces and slow structure equilibration. Un-ligated and self-ligated Hi-C artifacts do not contain information about the 3D organization of the chromosome; they are short range contacts that map entirely within a single Hi-C bin (main diagonal), or across one Hi-C bin boundary (1st off-diagonal) (16). To accelerate CSynth structure equilibration, the ratio of main diagonal contact probabilities to off-diagonal contact probabilities was set to 100 by dividing main diagonal contact probabilities by a constant, and the ratio of 1st off-diagonal contact probabilities to off-diagonal contact probabilities was set to 10 by dividing 1st off-diagonal contact probabilities by a constant. These modifications were chosen such that after normalization, CSynth Hi-C attraction forces remained high enough to allow structure equilibration within minutes. Main diagonal and 1st off-diagonal contact probabilities were excluded for all contact probability curve calculations.

Individual Hi-C contact files for each chromosome were then ICE normalized (65) and written to a text file in a CSynth compatible format via the cooler python package (66).

Generating 3D chromosome conformations with CSynth. CSynth was accessed online at: https://csynth.github.io/csynth/csynth.html (27). The maximum number of monomers supported by our system's GPU was determined by typing the command gl.getParameter(gl.MAX_TEXTURE_SIZE) into the console of the web browser's developer tools.

The following optimized parameters (SI Appendix, Fig. S3) were used:

- Spring power: 0. This sets the relative importance of long and short distance effects.
- Contact force: 60. This sets the magnitude of attraction between Hi-C contacts.
- Push-apart power: -4. This sets the exponent for a global repulsive force between monomers that decays with distance.

After equilibration, the xyz coordinates of all monomers were saved to a text file. A picture of the equilibrated structure was saved separately.

Simulated CLC Hi-C contact maps. 3D polymer models of CLCs were generated using a custom MATLAB script. Polymer length (20 Mb, 4000 monomers) was chosen to match the largest *S. microadriaticum* and *S. kawagutii* Hi-C scaffolds. After specifying the fraction of total monomers in extrachromosomal loops, and the fraction of loop monomers in inter-disc loops (1 - the fraction of monomers in intra-disc loops, (SI Appendix, Fig. S1 A)), the remaining monomers were divided by the number of cholesteric discs -1 to give the mean inter-disc loop length. Inter-disc loop lengths were then drawn from an exponential distribution with a parameter determined by the mean inter-disc loop length. This was done to make loop starts/stops as uniformly distributed in monomer space as possible. Intra-disc extrachromosomal loop lengths were drawn from an analogous distribution. Hi-C contacts were simulated using $CP_{Hi-C,ij} \propto 1/(D_{ij})^4$ (67), where $CP_{Hi-C,ij}$ represents the Hi-C contact probability for genomic loci pair (i, j), and D_{ij} represents the Euclidean distance between these two monomers. For population level Hi-C contact maps, the contact probability for each single-conformation Hi-C contact map was averaged per pixel (i, j) across all conformations.

Human control Hi-C and FISH data. Human IMR90 Hi-C data (28) were accessed from the GEO using accession number: GSE63525. IMR90 FISH probe 3D locations (29) were downloaded from: https://doi.org/10.5281/zenodo.3928890.

Equilibrium globule structures. Equilibrium globule structures were downloaded from GEO using the accession number: GSE18199 (33).

Spatial organization of transcription analysis. RNA-seq data from asynchronous cell populations were accessed via the SRA using the following accession numbers: for *S. microadriaticum*, SRR3337493 (24); for *S. kawagutii*, SRR9417753, SRR9417755, SRR9417756, SRR1300302, SRR1300303, SRR1300304, and SRR1300305 (25, 26).

Alignment to the genome assembly was performed following the methods outlined in (17).

Normalized gene density calculation. The largest 75 chromosome scaffolds for each dinoflagellate species were scaled isotropically to the same size, with each chromosome long axis aligned horizontally. Using a cylindrical coordinate system, the total number of RNA-seq reads were counted in each voxel, integrated azimuthally, and divided by the cylindrical Jacobian which controls for variation in amount of DNA per voxel.

DRAFT

Manual annotation of TADs using CSynth. After loading a Hi-C contact file into CSynth, we unchecked "ribbon" and "simulation" in the GUI's drop-down menu which hides the chromosome and arrests dynamics, respectively. We selected the matrix to display Hi-C contacts by using the menu: matrix→color→input A: "name of Hi-C file". We adjusted the *matdistfar* parameter until TADs were clearly visible. For a more upright matrix view, we increased matrix→rotation to 1.5. To annotate a TAD, we selected the TAD apex using the mouse, and edges appeared outlining the TAD boundary. We pressed option+Z to save the TAD coordinates and repeated for other TADs. We then pressed shift+option+Z to download a .bed file with the TAD start/end basepair coordinates as rows. To clear the memory of TAD coordinates, we pressed and held M then pressed zero. To color TADs in 3D, after re-checking "ribbon", the .bed file was dragged and dropped into the CSynth browser window.

TAD asphericity calculation. Asphericity is defined as in (37): $Asphericity = \frac{3}{2\left(\sum_{i=1}^{3}\lambda_i\right)^2}\sum_{i=1}^{3}(\lambda_i - <\lambda>)^2$,

where λ are the sorted $(\lambda_1 > \lambda_2 > \lambda_3)$ eigenvalues of the gyration tensor G, where

$$G = \frac{1}{N}\begin{pmatrix} \sum_{i=1}^{N}(x_i-x_{cm})^2 & \sum_{i=1}^{N}(x_i-x_{cm})(y_i-y_{cm}) & \sum_{i=1}^{N}(x_i-x_{cm})(z_i-z_{cm}) \\ \sum_{i=1}^{N}(x_i-x_{cm})(y_i-y_{cm}) & \sum_{i=1}^{N}(y_i-y_{cm})^2 & \sum_{i=1}^{N}(y_i-y_{cm})(z_i-z_{cm}) \\ \sum_{i=1}^{N}(x_i-x_{cm})(z_i-z_{cm}) & \sum_{i=1}^{N}(y_i-y_{cm})(z_i-z_{cm}) & \sum_{i=1}^{N}(z_i-z_{cm})^2 \end{pmatrix}$$

In this equation, N is the number of monomers and x_{cm}, y_{cm}, z_{cm} is the centres of mass. Asphericity is 0 when monomers are arranged as a perfect sphere and 1 when monomers are arranged as a perfect rod.

Data Availability

Code is available at: https://github.com/lucasphilipp1/3D-Reconstruction-of-Dinoflagellate-Chromosomes-from-Hi-C-Data. *S. kawagutii* Hi-C data, *S. kawagutii* and *S. microadriaticum* CSynth conformations, CLC structures, RNA-seq .bed files, and TAD .bed files, have been deposited to https://doi.org/10.5281/zenodo.14285613.

Supporting Information Appendix (SI)

Supporting Information accompanying this article including Figures S1-S10 and Tables S1-S3 can be found here https://www.pnas.org/cgi/doi/10.1073/pnas.XXXXXXXXXX.

ACKNOWLEDGMENTS. We would like to thank Audrey Baguette for helpful discussions regarding Hi-C data pre-processing. L.P. was supported by a Canadian Graduate Scholarship – Master's and a Canadian Graduate Scholarship – Doctoral from the National Science and Engineering Research Council of Canada. The work was funded by the New Frontiers in Research Fund (NFRFE-2019-00189 to S.C.W.).

References.

1. Y Bhaud, et al., Morphology and behaviour of dinoflagellate chromosomes during the cell cycle and mitosis. *J. Cell Sci.* **113**, 1231–1239 (2000).
2. E Miron, et al., Chromatin arranges in chains of mesoscale domains with nanoscale functional topography independent of cohesin. *Sci. Adv.* **6**, eaba8811 (2020).
3. JK Chen, et al., Nanoscale analysis of human G1 and metaphase chromatin in situ. *bioRxiv* **1** (2023).
4. KC Palozola, et al., Mitotic transcription and waves of gene reactivation during mitotic exit. *Science* **358**, 119–122 (2017).
5. Y Bouligand, M Soyer, S Puiseux-Dao, La structure fibrillaire et l'orientation des chromosomes chez les dinoflagellés. *Chromosoma* **24**, 251–287 (1968).
6. F Livolant, Y Bouligand, New observations on the twisted arrangement of dinoflagellate chromosomes. *Chromosoma* **68**, 21–44 (1978).
7. A Gautier, L Michel-Salamin, E Tosi-Couture, A McDowall, J Dubochet, Electron microscopy of the chromosomes of dinoflagellates in situ: confirmation of Bouligand's liquid crystal hypothesis. *J. Ultrastruct. Mol. Struct. Res.* **97**, 10–30 (1986).
8. RL Rill, F Livolant, HC Aldrich, MW Davidson, Electron microscopy of liquid crystalline DNA: direct evidence for cholesteric-like organization of DNA in dinoflagellate chromosomes. *Chromosoma* **98**, 280–286 (1989).
9. Y Bouligand, V Norris, Chromosome separation and segregation in dinoflagellates andbacteria may depend on liquid crystalline states. *Biochimie* **83**, 187–192 (2001).
10. DC Sigee, Structural DNA and genetically active DNA in dinoflagellate chromosomes. *Biosystems* **16**, 203–210 (1983).
11. DC Sigee, The dinoflagellate chromosome. *Adv. Bot. Res.* **12**, 205–264 (1986).
12. MO Soyer-Gobillard, The genome of the primitive eukaryote dinoflagellates: organization and functioning. *Zool. Stud.* **35**, 78–84 (1996).
13. MH Chow, KT Yan, MJ Bennett, JT Wong, Birefringence and DNA condensation of liquid crystalline chromosomes. *Eukaryot. Cell* **9**, 1577–1587 (2010).
14. JH Wisecaver, JD Hackett, Dinoflagellate genome evolution. *Annu. Rev. Microbiol.* **65**, 369–387 (2011).
15. S Riaz, Z Niaz, S Khan, Y Liu, Z Sui, Detection, characterization and expression dynamics of histone proteins in the dinoflagellate *Alexandrium pacificum* during growth regulation. *Harmful Algae* **87**, 101630 (2019).
16. A Nand, et al., Genetic and spatial organization of the unusual chromosomes of the dinoflagellate *Symbiodinium microadriaticum*. *Nat. Genet.* **53**, 618–629 (2021).
17. GK Marinov, et al., Transcription-dependent domain-scale three-dimensional genome organization in the dinoflagellate *Breviolum minutum*. *Nat. Genet.* **53**, 613–617 (2021).
18. GK Marinov, A Kundaje, WJ Greenleaf, AR Grossman, Protocol for mapping the three-dimensional organization of dinoflagellate genomes. *STAR Protoc.* **5**, 102941 (2024).
19. M Aranda, et al., Genomes of coral dinoflagellate symbionts highlight evolutionary adaptations conducive to a symbiotic lifestyle. *Sci. Reports* **6**, 39734 (2016).
20. TG Stephens, et al., Genomes of the dinoflagellate *Polarella glacialis* encode tandemly repeated single-exon genes with adaptive functions. *BMC Biol.* **18**, 1–21 (2020).
21. TR Bachvaroff, AR Place, From stop to start: tandem gene arrangement, copy number and trans-splicing sites in the dinoflagellate *Amphidinium carterae*. *PLoS One* **3**, e2929 (2008).
22. M Beauchemin, et al., Dinoflagellate tandem array gene transcripts are highly conserved and not polycistronic. *Proc. Natl. Acad. Sci.* **109**, 15793–15798 (2012).
23. TC LaJeunesse, et al., Systematic revision of Symbiodiniaceae highlights the antiquity and diversity of coral endosymbionts. *Curr. Biol.* **28**, 2570–2580 (2018).
24. YJ Liew, Y Li, S Baumgarten, CR Voolstra, M Aranda, Condition-specific RNA editing in the coral symbiont *Symbiodinium microadriaticum*. *PLoS Genet.* **13**, e1006619 (2017).
25. T Li, et al., RNA-seq profiling of *Fugacium kawagutii* reveals strong responses in metabolic processes and symbiosis potential to deficiencies of iron and other trace metals. *Sci. Total. Environ.* **705**, 135767 (2020).
26. PJ Keeling, et al., The marine microbial eukaryote transcriptome sequencing project (MMETSP): illuminating the functional diversity of eukaryotic life in the oceans through transcriptome sequencing. *PLoS Biol.* **12**, e1001889 (2014).
27. S Todd, et al., Csynth: an interactive modelling and visualization tool for 3D chromatin structure. *Bioinformatics* **37**, 951–955 (2021).
28. SS Rao, et al., A 3D map of the human genome at kilobase resolution reveals principles of chromatin looping. *Cell* **159**, 1665–1680 (2014).
29. JH Su, P Zheng, SS Kinrot, B Bintu, X Zhuang, Genome-scale imaging of the 3D organization and transcriptional activity of chromatin. *Cell* **182**, 1641–1659 (2020).
30. CS Yen, RE Steele, PMM Rae, Chromatin structure in a dinoflagellate as revealed by electron microscopy of DNA cross-linked in vivo with trimethylpsoralen. *J. Cell Biol.* **79**, 120a (1978).
31. T Li, et al., Genome improvement and core gene set refinement of *Fugacium kawagutii*. *Microorganisms* **8**, 102 (2020).
32. TJ Stevens, et al., 3D structures of individual mammalian genomes studied by single-cell Hi-C. *Nature* **544**, 59–64 (2017).
33. E Lieberman-Aiden, et al., Comprehensive mapping of long-range interactions reveals folding principles of the human genome. *Science* **326**, 289–293 (2009).
34. N Naumova, et al., Organization of the mitotic chromosome. *Science* **342**, 948–953 (2013).
35. Open2C, et al., Cooltools: enabling high-resolution Hi-C analysis in Python. *PLOS Comput. Biol.* **20**, e1012067 (2024).
36. J Xu, et al., A comprehensive benchmarking with interpretation and operational guidance for the hierarchy of topologically associating domains. *Nat. Commun.* **15**, 4376 (2024).
37. W Huang, V Zaburdaev, The shape of pinned forced polymer loops. *Soft Matter* **15**, 1785–1792 (2019).
38. B Zhang, PG Wolynes, Topology, structures, and energy landscapes of human chromosomes. *Proc. Natl. Acad. Sci.* **112**, 6062–6067 (2015).
39. GA Orsi, et al., Biophysical ordering transitions underlie genome 3D re-organization during cricket spermiogenesis. *Nat. Commun.* **14**, 4187 (2023).
40. C Babillot, Étude de l'incorporation d'uridine-^{3}H dans le noyau chez l'*Amphidinium carteri*, dinoflagellé. *C. R. Acad. Sci. (Paris)* **271**, 828–831 (1970).
41. M Sala-Rovira, et al., Molecular cloning and immunolocalization of two variants of the major basic nuclear protein (HCc) from the histone-less eukaryote *Crypthecodinium cohnii* (Pyrrhophyta). *Chromosoma* **100**, 510–518 (1991).
42. ML Géraud, M Sala-Rovira, M Herzog, MO Soyer-Gobillard, Immunocytochemical localization of the dna-binding protein HCc during the cell cycle of the histone-less dinoflagellate protoctista *Crypthecodinium cohnii B. Biol. Cell* **71**, 123–134 (1991).
43. DM Anderson, A Grabber, M Herzog, Separation of coding sequences from structural DNA in the dinoflagellate *Crypthecodinium cohnii. Mol. Mar. Biol. Biotechnol.* **1**, 89–96 (1992).
44. D Spector, A Vasconcelos, R Triemer, DNA duplication and chromosome structure in the dinoflagellates. *Protoplasma* **105**, 185–194 (1981).

DRAFT

45. BR Oakley, JD Dodge, Evidence for a double-helically coiled toroidal chromonema in the dinoflagellate chromosome. *Chromosoma* **70**, 277–291 (1979).
46. O Haapala, MO Soyer, Structure of dinoflagellate chromosomes. *Nat. New Biol.* **244**, 195–197 (1973).
47. M Herzog, M Soyer, The native structure of dinoflagellate chromosomes and their stabilization by Ca2+ and Mg2+ cations. *Eur. J. Cell Biol.* **30**, 33–41 (1983).
48. JD Dodge, The chromosomes of dinoflagellates in *International Review of Cytology*. (Elsevier) Vol. 94, pp. 5–19 (1985).
49. JTY Wong, Architectural organization of dinoflagellate liquid crystalline chromosomes. *Microorganisms* **7**, 27 (2019).
50. TB Le, MV Imakaev, LA Mirny, MT Laub, High-resolution mapping of the spatial organization of a bacterial chromosome. *Science* **342**, 731–734 (2013).
51. KP Eagen, TA Hartl, RD Kornberg, Stable chromosome condensation revealed by chromosome conformation capture. *Cell* **163**, 934–946 (2015).
52. VG Contessoto, et al., Interphase chromosomes of the *Aedes aegypti* mosquito are liquid crystalline and can sense mechanical cues. *Biophys. J.* **122**, 20a (2023).
53. B Yee, E Sagulenko, GP Morgan, RI Webb, JA Fuerst, Electron tomography of the nucleoid of *Gemmata obscuriglobus* reveals complex liquid crystalline cholesteric structure. *Front. Microbiol.* **3**, 326 (2012).
54. B Yee, E Sagulenko, JA Fuerst, Making heads or tails of the HU proteins in the planctomycete *Gemmata obscuriglobus*. *Microbiology* **157**, 2012–2021 (2011).
55. SG Gornik, et al., Loss of nucleosomal DNA condensation coincides with appearance of a novel nuclear protein in dinoflagellates. *Curr. Biol.* **22**, 2303–2312 (2012).
56. GK Marinov, et al., Genome-wide distribution of 5-hydroxymethyluracil and chromatin accessibility in the *Breviolum minutum* genome. *Genome Biol.* **25**, 115 (2024).
57. D Saintillan, MJ Shelley, A Zidovska, Extensile motor activity drives coherent motions in a model of interphase chromatin. *Proc. Natl. Acad. Sci.* **115**, 11442–11447 (2018).
58. J Allen, TM Roberts, AR Loeblich III, LC Klotz, Characterization of the DNA from the dinoflagellate *Crypthecodinium cohnii* and implications for nuclear organization. *Cell* **6**, 161–169 (1975).
59. JW Udy, R Hinde, M Vesk, Chromosomes and DNA in *Symbiodinium* from Australian hosts. *J. Phycol.* **29**, 314–320 (1993).
60. KD Weynberg, et al., Prevalent and persistent viral infection in cultures of the coral algal endosymbiont *Symbiodinium*. *Coral Reefs* **36**, 773–784 (2017).
61. G Sergey, B Mariia, M Yana, S Eugene, S Sergei, Ultrastructural organization of the chromatin elements in chromosomes of the dinoflagellate *Prorocentrum minimum*. *Protistology* **12**, 163–172 (2018).
62. I Sunesen, et al., Morphological and molecular characterization of *Heterocapsa claromecoensis* sp. nov. (Peridiniales, Dinophyceae) from Buenos Aires coastal waters (Argentina). *Eur. J. Phycol.* **55**, 490–506 (2020).
63. G Costas, E., V J., Ultrastructure and division behaviour of dinoflagellate chromosomes. *Chromosom. (Berl)* **95**, 435–441 (1987).
64. P Le, N Ahmed, GW Yeo, Illuminating RNA biology through imaging. *Nat. Cell Biol.* **24**, 815–824 (2022).
65. M Imakaev, et al., Iterative correction of Hi-C data reveals hallmarks of chromosome organization. *Nat. Methods* **9**, 999–1003 (2012).
66. N Abdennur, LA Mirny, Cooler: scalable storage for Hi-C data and other genomically labeled arrays. *Bioinformatics* **36**, 311–316 (2020).
67. S Wang, et al., Spatial organization of chromatin domains and compartments in single chromosomes. *Biophys. J.* **112**, 217a (2017).

DRAFT